

Using Nanoparticle X-ray Spectroscopy to Probe the Formation of Reactive Chemical Gradients in Diffusion-Limited Aerosols

Michael I. Jacobs,^{†,‡,Ⓜ} Bo Xu,^{‡,Ⓜ} Oleg Kostko,^{‡,Ⓜ} Aaron A. Wiegel,[‡] Frances A. Houle,^{‡,Ⓜ} Musahid Ahmed,^{‡,Ⓜ} and Kevin R. Wilson^{*,‡,Ⓜ}

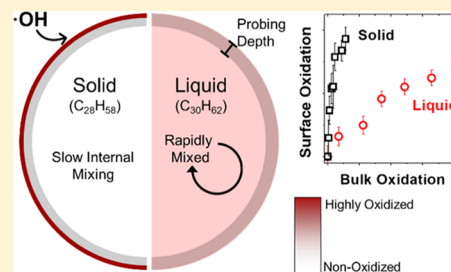
[†]Department of Chemistry, University of California, Berkeley, California 94720, United States

[‡]Chemical Sciences Division, Lawrence Berkeley National Laboratory, Berkeley, California 94720, United States

S Supporting Information

ABSTRACT: For aerosol particles that exist in highly viscous, diffusion-limited states, steep chemical gradients are expected to form during photochemical aging in the atmosphere. Under these conditions, species at the aerosol surface are more rapidly transformed than molecules residing in the particle interior. To examine the formation and evolution of chemical gradients at aerosol interfaces, the heterogeneous reaction of hydroxyl radicals (OH) on ~200 nm particles of pure squalane (a branched, liquid hydrocarbon) and octacosane (a linear, solid hydrocarbon) and binary mixtures of the two are used to understand how diffusion limitations and phase separation impact the particle reactivity. Aerosol mass spectrometry is used to measure the effective heterogeneous OH uptake

coefficient (γ_{eff}) and oxidation kinetics in the bulk, which are compared with the elemental composition of the surface obtained using X-ray photoemission. When diffusion rates are fast relative to the reaction frequency, as is the case for squalane and low-viscosity squalane–octacosane mixtures, the reaction is efficient ($\gamma_{\text{eff}} \sim 0.3$) and only limited by the arrival of OH to the interface. However, for cases, where the diffusion rates are slower than reaction rates, as in pure octacosane and higher-viscosity squalane–octacosane mixtures, the heterogeneous reaction occurs in a mixing-limited regime and is $\sim 10\times$ slower ($\gamma_{\text{eff}} \sim 0.03$). This is in contrast to carbon and oxygen K edge X-ray absorption measurements that show that the octacosane interface is oxidized much more rapidly than that of pure squalane particles. The O/C ratio of the surface (estimated to be the top 6–8 nm of the interface) is measured to change with rate constants of $(3.0 \pm 0.9) \times 10^{-13}$ and $(8.6 \pm 1.2) \times 10^{-13}$ $\text{cm}^3 \text{molecule}^{-1} \text{s}^{-1}$ for squalane and octacosane particles, respectively. The differences in surface oxidation rates are analyzed using a previously published reaction-diffusion model, which suggests that a 1–2 nm highly oxidized crust forms on octacosane particles, whereas in pure squalane, the reaction products are homogeneously mixed within the aerosol. This work illustrates how diffusion limitations can form particles with highly oxidized surfaces even at relatively low oxidant exposures, which is in turn expected to influence their microphysics in the atmosphere.



I. INTRODUCTION

Recent work provides evidence that atmospheric aerosol particles exist in solid, liquid, and highly viscous, diffusion-limited phase states, with viscosities ranging from $<10^2$ to $>10^8$ Pa s.^{1–4} Atmospheric aerosols are transformed by photochemical reactions, heterogeneous oxidation, and condensation of low-volatility organic species to yield increasingly oxidized, less volatile, and more hygroscopic particles.⁵ Chemical gradients are expected to form in semisolid, highly viscous particles as they age in the atmosphere leading to more rapid changes in the surface composition and potentially affecting their atmospheric fates. For example, rapidly changing the chemical nature of the aerosol surface could influence its ability to act as a cloud condensation nucleus.^{6–9} Because steep chemical gradients in aerosol could change its chemistry with atmospheric trace gases, it is important to understand the formation of chemical gradients and the chemical nature of the interface.

The viscosity and the phase state of an aerosol particle or a film have been measured to have a significant effect on

heterogeneous oxidation kinetics.^{10–21} Many species can exist as amorphous semisolids or glasses with very slow internal diffusion at low relative humidity (RH) or low temperature, which has been observed to slow heterogeneous oxidation kinetics.^{10,11,14–18} For example, heterogeneous oxidation kinetics of levoglucosan were found to slow with decreasing relative humidity, which decreased reactodiffusive lengths.¹¹ Additionally, a study found the effective uptake coefficient of squalane ($\text{C}_{30}\text{H}_{62}$, a branched hydrocarbon that is liquid at room temperature) to be significantly larger than octacosane ($\text{C}_{28}\text{H}_{58}$, a linear hydrocarbon that is solid at room temperature) even though the individual molecules were estimated to have similar reactivity with the OH radical.¹⁹ The product distribution was also different for squalane and octacosane. While squalane showed functionalization throughout the molecule, octacosane was only functionalized at the

Received: May 12, 2019

Revised: June 19, 2019

Published: June 21, 2019

ends of the molecules. This suggested that while squalane was free to diffuse and rotate in the particle, octacosane molecules experienced “surface freezing”, wherein the linear alkane chains preferentially orient normal to the surface.^{19,22} Because the OH radical reacts at the top ~ 1 nm in organic aerosol,²³ the differences in effective uptake coefficients were attributed to differences in phase state and the ability for molecules to diffuse to the interface to react.

Recent modeling results have focused on how diffusion limitations can lead to emergent properties of aerosol particles.^{16,24–27} The overall reactivity of an aerosol particle to heterogeneous oxidation is a balance between the flux of oxidant at the surface and the internal mixing dynamics. To understand the reactivity across a broad range of diffusion coefficients, a reaction-diffusion index (I_{RD}), also known as the Damköhler number, has been defined by Houle et al. to be^{25,26}

$$I_{RD} = k_{rx}[\text{gas}]\tau_{cd} \quad (1)$$

where k_{rx} is the rate constant for the reaction between gas-phase oxidant and species in the particle, $[\text{gas}]$ is the concentration of gas-phase oxidant, and τ_{cd} is the characteristic mixing time, which is proportional to the square of the particle diameter and inversely proportional to the molecular diffusion coefficient. If $I_{RD} \ll 1$, then mixing is fast relative to the arrival of the gas-phase oxidant to the aerosol surface, and the supply of OH limits the reaction. If $I_{RD} \gg 1$, then the internal mixing rate to refresh molecules at the aerosol surface is rate limiting. Thus, even though the reactive uptake coefficient of a particle may be constant, changes in its bulk composition and the measured effective uptake coefficient will depend upon the exact experimental time scales (i.e., laboratory vs atmosphere). At larger I_{RD} , bulk composition changes much more slowly, and large chemical gradients form within the particle as the surface becomes more highly oxidized than the bulk.^{14,18} For this study, two extremes of I_{RD} are examined. To do this, two structurally related molecules are selected with similar OH reactivity but with mixing times that are orders of magnitude different.

The techniques that are commonly used to study aerosols, such as aerosol mass spectrometry,²⁸ scanning transmission X-ray microscopy,²⁹ scanning electron microscopy,³⁰ and chromatographic methods coupled with mass spectrometry,³¹ probe volume-weighted aerosol chemistry. These techniques measure average bulk composition or micron-scale heterogeneity but are unable to detect the nanoscale spatial heterogeneity that is expected to form in diffusion-limited aerosol particles. By reacting coated aerosols, there has been some work to determine how spatial heterogeneity can affect oxidation kinetics.³² There has also been work to develop analytical techniques that are more surface sensitive and can measure spatial heterogeneity within aerosol particles. For example, depth profiling of aerosol particles was achieved by introducing a particle stream into a heated gas stream and only ionizing/detecting the gas-phase species that evaporated from the particle surface.^{14,33–35} Additionally, surface sensitivity has been achieved by using extractive electrospray ionization to desorb and ionize molecular species from the aerosol interface.^{36,37} Surface sensitivity has also been achieved using nonlinear spectroscopic techniques, such as second harmonic scattering from free aerosol particles³⁸ or sum frequency generation from aerosol collected onto a filter substrate.^{39,40} However, there are few online, universally surface sensitive

measurements that can measure the formation and dissipation of chemical gradients within a particle in situ.

Photoemission spectroscopy is a universally surface sensitive measurement because of the short electron attenuation length (EAL) in materials. The study of photoemission from free aerosol particles is still in its infancy.⁴¹ Several experiments have used ultraviolet photoelectron spectroscopy (UPS) to study the electronic structure of free nanoparticles.^{42–53} Many of these studies have used a velocity map imaging (VMI) spectrometer to image a projection of the nascent photoelectron distribution of low-energy electrons that originated from valence energy levels.^{42,43,46–53} Additionally, X-ray photoelectron spectroscopy (XPS) studies have probed free nanoparticles to provide elemental information of the surface.^{51,54–62} Photoemission spectroscopy, UPS, XPS, and X-ray absorption spectroscopy (XAS), has previously been used to study the surfaces of liquid squalene aerosol particles during a surface reaction with ozone.⁵¹ However, photoemission spectroscopy has not been used to study heterogeneous chemistry in particles with diffusion limitations, wherein the reaction is expected to exhibit substantial spatial heterogeneity.

The heterogeneous oxidation of triacontane ($C_{30}H_{62}$, a linear hydrocarbon) has been previously studied using an aerosol mass spectrometer to probe changes in bulk composition.^{63,64} Using a reaction-diffusion kinetic model, it was predicted that under laboratory conditions, the surface of the particle was oxidized much more rapidly than the bulk (i.e., $I_{RD} \gg 1$).⁶⁴ Here, photoemission is used to probe the surface reaction of OH on squalane and octacosane particles, which represent two limiting cases for studying the formation of chemical gradients: $I_{RD} \ll 1$ (squalane) and $I_{RD} \gg 1$ (octacosane).

II. EXPERIMENTAL METHODS

The experimental setup used to study OH radical heterogeneous chemistry was nearly identical to that described previously^{51,65} and is shown in Figure 1. Briefly, particles are generated by flowing nitrogen through a heated reservoir containing either squalane, octacosane, or a mixture of the two

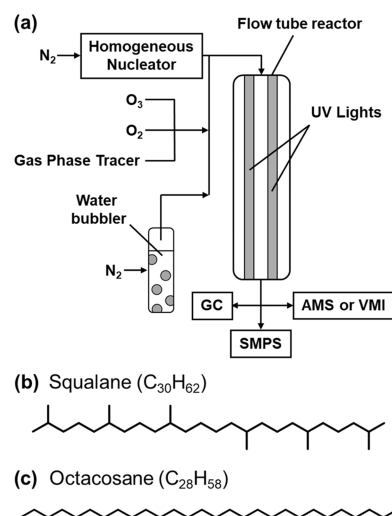


Figure 1. (a) Schematic of flow tube setup (GC = gas chromatograph, SMPS = scanning mobility particle sizer, AMS = VUV aerosol mass spectrometer, VMI = velocity map imaging spectrometer). The chemical structures of squalane (b) and octacosane (c).

(molecular structures are shown in Figure 1b,c). After the oven, particles pass through an additional length of heated tubing (~ 80 °C) for annealing in an effort to make the particles more spherical. The particle flow was mixed with oxygen (10%), humidified nitrogen (30%), dry nitrogen, ozone, and a gas-phase OH tracer (~ 0.5 ppm acetone). The total flow rate was ~ 1000 sccm. The particle concentrations were typically $\sim 1 \times 10^6$ and $5\text{--}10 \times 10^6$ particles cm^{-3} for mass spectrometry and photoemission measurements, respectively. The flow was introduced into a quartz flow tube (2.5 cm inner diameter, 140 cm length). Particles had an average residence time of ~ 37 s in the flow tube. The particles were oxidized by the OH radical, generated within the flow tube by the photolysis of ozone in the presence of water vapor using mercury lamps at 254 nm. After the flow tube, the concentration of the gas-phase tracer was measured using a gas chromatograph (GC). From the decay of acetone and its OH reaction rate constant ($k_{\text{acetone}} = 1.8 \times 10^{-13}$ cm^3 molecule^{-1} s^{-1}),⁶⁶ the OH exposure ($\langle \text{OH} \rangle_t t$) was calculated. A scanning mobility particle sizer (SMPS) after the flow tube quantified changes in the particle size distribution with oxidation.

The bulk chemical composition of the aerosol was measured using a vacuum ultraviolet aerosol mass spectrometer (VUV-AMS).⁶⁷ The particles were collimated using an aerodynamic lens (ADL) and vaporized on a 135 °C heated block. The resulting vapor was ionized using 10.2 eV photons from the Chemical Dynamics Beamline (9.0.2) at the Advanced Light Source (ALS) at Lawrence Berkeley National Laboratory. The effective uptake coefficients of particles comprised of pure squalane, pure octacosane, and mixtures of the two were determined, as previously described.⁶⁵ Details are provided in the Supporting Information.

The aerosol surface composition was probed by XPS and XAS. Specifically, XPS was used to study the heterogeneous oxidation of pure squalane particles by the OH radical, and XAS at the carbon and oxygen K edges was used to study the heterogeneous oxidation of pure squalane and octacosane particles. The details of these measurements have been described previously.^{51,60} Briefly, particles were introduced into a velocity map imaging (VMI) spectrometer via an ADL, and photoelectrons were mapped onto a multichannel plate (MCP)/phosphor detector.⁶⁰ C 1s XPS spectra were obtained using a photon energy of 330 eV. Particle and background images were collected for 300 s, and a photoelectron spectrum from the background-subtracted images was obtained using conventional techniques.⁶⁸ XAS spectra were collected by scanning the incident photon energy and measuring the intensity of low kinetic energy (KE), secondary electrons (KE < 10 eV) that are generated by inelastic scattering of Auger electrons. A photomultiplier tube was used to measure the total electron yield (TEY) from the MCP-phosphor detector. Carbon and oxygen K edge XAS spectra were collected from 280 to 300 eV and 526 to 552 eV, respectively. The spectra were collected with 0.2 eV steps and exposure time of 1 s per step. X-ray measurements were done at the beamline 6.0.2 at the ALS.

III. RESULTS AND DISCUSSION

III.1. Bulk Squalane and Octacosane Particle Measurements. Aerosol mass spectra of pure squalane and octacosane are shown in Figure 2a,b, respectively. The mass spectra of squalane and octacosane have molecular ions at m/z 422 and

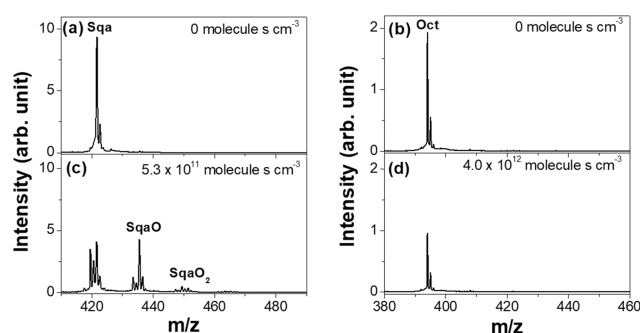


Figure 2. (a) Aerosol mass spectrum of squalane particles without exposure to OH radicals. The molecular ion is labeled as “Sqa”. (b) The mass spectrum of octacosane particles without exposure to OH radicals. The molecular ion is labeled as “Oct”. (c) The mass spectrum when about half of the squalane has reacted. Functionalized products with increasing numbers of oxygen (SqaO and SqaO₂) are present. (d) The mass spectrum when about half of the octacosane has reacted. No products are observed when octacosane heterogeneously reacts.

394, respectively. As the particles react with OH, the intensities of the molecular ions decrease. Although surface freezing of octacosane drives the chemistry through aldehydes, the same peroxy radical chemistries are expected to occur in squalane and octacosane (shown in Figure S1 of the Supporting Information).^{19,25,64} After the H-atom abstraction by OH, peroxy radicals are formed via O₂ addition to an alkyl radical. The subsequent reaction pathways of peroxy radicals typically form carbonyl and alcohol functional groups. Figure 2c shows the mass spectrum of squalane after about half of the initial concentration of squalane reacted (OH exposure is 5.3×10^{11} $\text{molecule s cm}^{-3}$). As the particles were heterogeneously oxidized by the OH radical, oxygenated products were detected and are consistent with previous observations.^{65,69,70}

Figure 2d shows the mass spectrum of octacosane after about half of its initial concentration is consumed (OH exposure is 4.0×10^{12} $\text{molecule s cm}^{-3}$). Octacosane reacts much more slowly than squalane (i.e., a much higher OH exposure is required to consume half of the octacosane). In addition, no functionalized products from heterogeneous oxidation are observed in the mass spectrum. This is consistent with previous observations, wherein the quantity of reaction products from octacosane after ~ 1 oxidation lifetime was substantially less intense than those observed from squalane oxidation.¹⁹ In this previous study, only the ends of the octacosane molecules reacted, suggesting that surface alignment and diffusion limitations allowed only the small number of molecules at the interface to react with OH. Thus, because the number of molecules at the interface is small relative to the bulk and the products are expected to be highly oxidized (which makes them more difficult to observe using the bulk sensitivity of the VUV photoionization technique), it is possible that the measurement here is not sensitive enough to observe the reaction products of octacosane.

The decay of the molecular ions at different OH exposures was monitored, and the effective uptake coefficients of pure squalane and octacosane were determined to be 0.31 ± 0.06 and 0.03 ± 0.01 , respectively. The uptake coefficient for squalane is very similar to previous measurements.^{19,65,71–73} Ruehl et al. previously measured an effective uptake coefficient of 0.18 ± 0.11 for octacosane,¹⁹ and Richards-Henderson et al. previously measured an effective uptake coefficient of ~ 0.17

for triacontane.^{72,73} Both of these measurements are larger than the value measured here. Since solid *n*-alkane particles form needle-like morphologies,⁷⁴ an annealing oven was used to melt the particles to make them more spherical, which helped with aerodynamic focusing in the spectrometer. Nonspherical particles have a larger surface area, which leads to larger OH collision frequencies and faster heterogeneous reaction rates. Because Ruehl et al. and Richards-Henderson et al. did not anneal the solid *n*-alkane particles, differences in the particle morphology (i.e., surface area) could explain the larger effective uptake coefficients reported in their work.

Given the distribution of abstractable H atoms in each molecule, the gas-phase reactivities of squalane and octacosane were estimated to be very similar ($k_{\text{gas}} = 4.0 \times 10^{-10}$ and 3.7×10^{-10} cm³ molecule⁻¹ s⁻¹, for squalane and octacosane, respectively).⁷⁵ Because particle size and OH concentration were similar for both experiments, differences in internal mixing times likely explain the large differences in effective uptake coefficient.²⁴ The self-diffusion coefficients in squalane⁷⁶ and triacontane⁶⁴ (a linear hydrocarbon very similar to octacosane) are 7×10^{-7} and 8.3×10^{-19} cm² s⁻¹, respectively. Thus, 200 nm aerosols comprised of squalane and octacosane will have characteristic mixing times of $\sim 10^{-5}$ and $\sim 10^7$ s, respectively. Based on the present reaction conditions, squalane and octacosane have I_{RD} of $\sim 10^{-7}$ and $\sim 10^5$, respectively, suggesting that these particles react in much different rate-limiting regimes (i.e., OH flux limited vs diffusion limited).^{25,26}

Figure 3 shows the effective uptake coefficients of octacosane and squalane measured in different squalane–octacosane mixtures. As the squalane mole fraction (x_{sqa}) increases, the octacosane molecular ion is observed to decay faster (Figure 3a). Figure 3b shows the computed effective uptake coefficients for octacosane and squalane as a function of

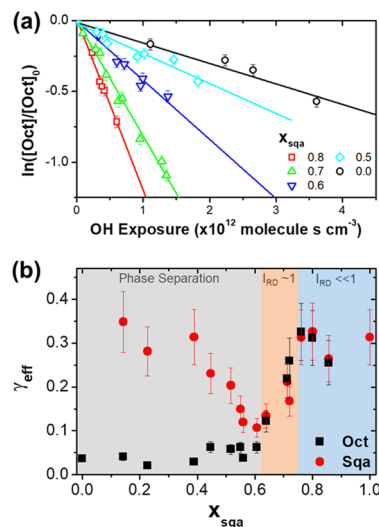


Figure 3. (a) Decay of the molecular ion of octacosane from heterogeneous oxidation in mixed octacosane–squalane particles with different compositions. (b) Calculated effective uptake coefficients of octacosane and squalane in mixtures of the two. The blue shaded region represents compositions where the reaction rate is OH flux limited ($I_{\text{RD}} \ll 1$). The orange shaded region represents compositions where diffusion limitations start to arise ($I_{\text{RD}} \sim 1$). The gray shaded region represents compositions where the particles are phase separated.

x_{sqa} . At higher concentrations of squalane ($x_{\text{sqa}} > 0.8$), the effective uptake coefficients of both octacosane and squalane are nearly identical to pure squalane, suggesting that diffusion is fast relative to reaction frequency (i.e., $I_{\text{RD}} \ll 1$ and that the reactions occur in an OH flux-limited regime). This is consistent with the two molecules having similar estimated reactivity toward OH, and the particles existing as a well-mixed liquid on the time scale of the heterogeneous reaction frequency.

As the concentration of squalane decreases ($0.6 < x_{\text{sqa}} < 0.8$), the particle becomes more viscous, and the effective uptake coefficients of both octacosane and squalane decrease. At these compositions, the viscosity in the particle increases, such that diffusion is slow relative to the reaction frequency. The decrease in measured effective uptake suggests that the particle is transitioning from an OH flux limited to a bulk diffusion-limited regime. In this transitory regime, the molecules in the aerosol interior become more inaccessible for the reaction at the interface. As diffusion continues to slow within the particle, ultimately only the molecules that reside within the reacto-diffusive length of OH (1–2 nm) react heterogeneously.²³ The heterogeneous oxidation of citric acid at different RHs showed a similar effect.¹⁴ At high RH, the viscosity of the citric acid particle was low, and the particle could mix freely (i.e., the reacto-diffusive length was larger than the radius of the particle and $I_{\text{RD}} \ll 1$). At lower RH, the viscosity decreased, and both the measured effective uptake coefficient and the reacto-diffusive length were smaller (i.e., $I_{\text{RD}} > 1$).

When the initial squalane composition decreases further ($x_{\text{sqa}} < 0.6$), the squalane and octacosane effective uptake coefficients diverge and approach the values measured in their pure states. The differences in the behavior of the molecular components suggest that at these mole fractions, the particles do not exist as a homogeneous mixture but rather are phase separated. Phase separation has been previously observed in particles composed of mixtures of solid and liquid components (such as mixtures of oleic acid and stearic acid).⁷⁴ Thus, by changing the composition of the particle, heterogeneous oxidation is observed to occur in either an OH flux limited (liquid well-mixed particles), organic mixing limited (semi-solid, viscous particles), or phase-separated regime.

III.II. X-ray Photoelectron Spectroscopy of Squalane Particles. X-ray photoelectron spectroscopy can measure average O/C (oxygen-to-carbon) ratios by directly probing the chemical composition of the surface.^{51,77} XPS spectra from the heterogeneous oxidation of squalane particles are shown in Figure 4. The spectra were collected with 330 eV photons (resulting in ~ 40 eV KE photoelectrons). An XPS spectrum of unoxidized squalane particles is shown in Figure 4a, and for comparison, an XPS spectrum of squalane oxidized at an OH exposure of 3.8×10^{12} molecule s cm⁻³ is shown in Figure 4b. The spectrum of oxidized squalane has a broad shoulder at higher binding energies, which is attributed to the formation of reaction products containing new oxygenated functional groups.

To extract a quantitative measure of the chemical composition of the surface of the particle, the XPS spectra were fit using a method adapted from previous studies.^{51,77} Since pure squalane is composed of only one type of carbon (methylene carbon, CH_x), a single Gaussian peak (FWHM = 2.0 eV) was first fit to the unoxidized squalane spectrum. Next, the most highly oxidized squalane spectrum was fit using two Gaussian peaks: the CH_x peak (which had the same parameters

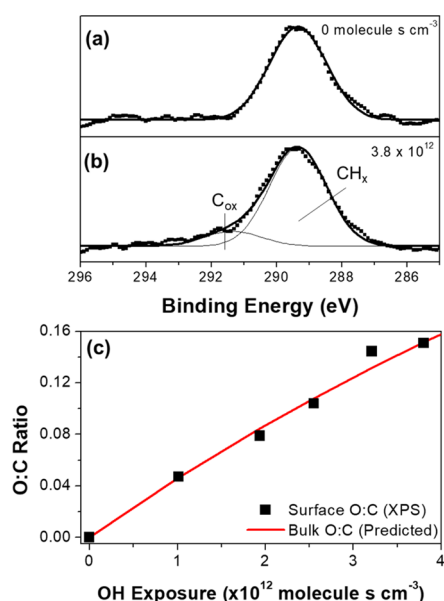


Figure 4. (a) and (b) show the XPS spectrum of squalane particles oxidized at OH exposure of 0 and 3.8×10^{12} molecule s^{-3} , respectively. Spectra were collected using 330 eV photons. (c) The measured O/C ratio at the surface of squalane at different OH exposures. Only one oxygen atom is associated with each C_{ox} (i.e., only ketones and alcohols formed). The O/C ratio of the bulk was predicted using kinetics measured in a previous work.⁷⁰

as in the unoxidized squalane spectrum) and an oxygenated carbon peak, C_{ox} (which was constrained to have the same FWHM as the CH_x peak). The C_{ox} peak was shifted by 2.0 eV relative to methylene CH_x peak, which is in good agreement with the average shift expected for carbonyls and alcohols.⁷⁸ The same two peaks were fit to the squalane spectra at each OH exposure. Based on the expected reaction products and the relative shift of the C_{ox} peak, only one oxygen atom is associated with each C_{ox} (i.e., only ketones and alcohols were formed).^{65,79} Thus, by monitoring the relative intensity of the C_{ox} peak, the O/C ratio at the surface could be measured directly (Figure 4c). The experimental O/C ratios are in good agreement with the bulk O/C ratios measured with an AMS from a previous study (shown as the red line in Figure 4c).⁷⁰

The O/C ratios measured with XPS were used to inform the X-ray absorption measurements, as described below. Unfortunately, we were unable to measure XPS spectra from octacosane particles. Even with annealing, it is suspected that the octacosane particles were not completely spherical and poorly collimated by the aerodynamic lens, leading to poor transmission efficiency and low XPS signal-to-noise ratio in the apparatus.

III.III. X-ray Absorption of Squalane and Octacosane Particles. XAS spectra at the carbon and oxygen K edges were collected by scanning the incident photon energy and measuring the intensity of low KE secondary electrons. An example distribution of low KE electrons from organic aerosol has been previously reported^{51,60} and is peaked around ~3 eV kinetic energy. Thus, based upon previous studies of the electron attenuation length in organic nanoparticles, the XAS measurements are expected to probe the topmost ~3–4 nm of the particle interface,⁵² as will be discussed in more detail below.

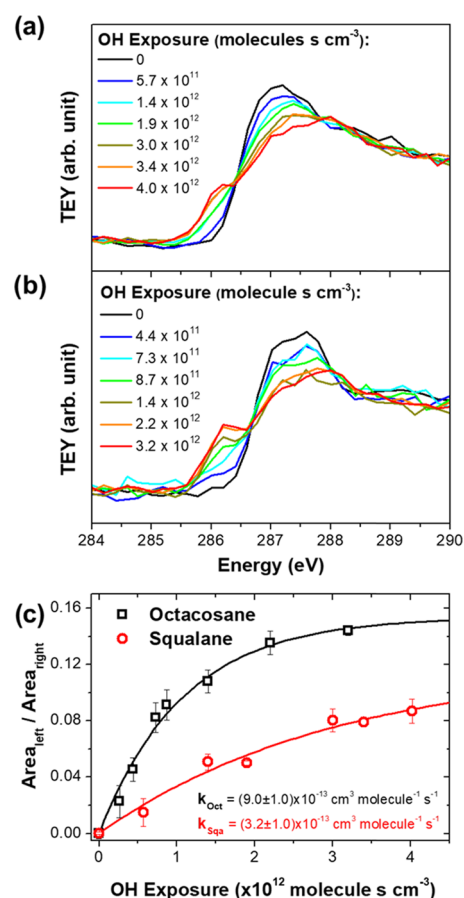


Figure 5. Carbon K edge XAS spectra of squalane (a) and octacosane (b) particles at different OH exposures. Spectra were area normalized using the measured TEY intensity from 286 to 300 eV. (c) Oxidation kinetics from carbon K edge XAS spectra was extracted by calculating the ratio of the area left of the isosbestic point (286.5 eV) to that right of the isosbestic point and plotting it as a function of OH exposure.

Figure 5 shows the carbon K edge XAS spectra of squalane and octacosane at different OH exposures. The spectra were area normalized using the TEY signal from 284 to 300 eV. For both particles, at higher OH exposures, a pre-edge feature at ~286 eV grows in, and the intensity at the initial pre-edge feature (~287 eV) decreases and blue shifts. The appearance of the pre-edge feature arises due to an increasing number of different functional groups at the particle surface.⁸⁰ Based on the reaction mechanism (Supporting Information, Figure S1), alcohols and carbonyls are likely contributors to this pre-edge feature for squalane (low I_{RD}), and carbonyls and carboxylic acids are likely contributors to this pre-edge feature for octacosane (high I_{RD}).²⁵ As shown by a comparison of gas-phase carbon K edge XAS spectra of ethane, ethanol, acetaldehyde, and acetic acid, the 1s C(CO) → π^* transition of carbonyls is the most likely assignment for this pre-edge spectral feature (Supporting Information, Figure S2).⁸¹ However, without XAS calculations, it is difficult to determine precisely which chemical species are responsible for all of the spectral changes observed.

Both the squalane and octacosane carbon K edge XAS spectra exhibit an isosbestic point at ~286.5 eV, indicating that there are at least two distinct populations of species that evolve during the reaction. Oxidation kinetics was extracted from the spectra by calculating the ratio of the spectral area to the left

and right of the isosbestic point as a function of OH exposure (Figure 5c). This method calculates the relative intensity of the pre-edge feature, which is assumed to be proportional to oxygenated products at the surface. As shown in Figure 5c, the pre-edge feature grows much more rapidly for octacosane than for squalane. A rate constant (k) describing the growth of a signal with increased oxidation was calculated using

$$I_t = I_{\max}(1 - e^{-k(\text{OH})_t}) \quad (2)$$

where I_t and I_{\max} are the signal intensity at a given OH exposure and the maximum possible signal intensity, respectively. The phenomenological rate constants for squalane and octacosane that best describe the kinetic rise of this pre-edge feature are $(3.2 \pm 1.0) \times 10^{-13}$ and $(9.0 \pm 1.0) \times 10^{-13} \text{ cm}^3 \text{ molecule}^{-1} \text{ s}^{-1}$, respectively. Since the starting diameters of squalane and octacosane were similar, both measured to be $\sim 200 \pm 40 \text{ nm}$, these heterogeneous rate constants can be directly compared. Thus, even though squalane appears much more reactive when observed with bulk sensitive probes, the surface of octacosane oxidizes $\sim 3\times$ faster. This measurement suggests that a chemical gradient forms during the oxidation of octacosane. However, because X-ray absorption at the carbon K edge probes the bonding environment around carbon atoms and changing speciation affects the shape of the spectrum, the magnitude of the chemical gradient cannot be determined by these data alone. Thus, direct probes of oxygenated species (such as oxygen K edge XAS) are necessary to quantify the absolute magnitudes of chemical gradients.

Figure 6 shows the oxygen K edge XAS spectra of squalane and octacosane as a function of OH exposure. The spectra are

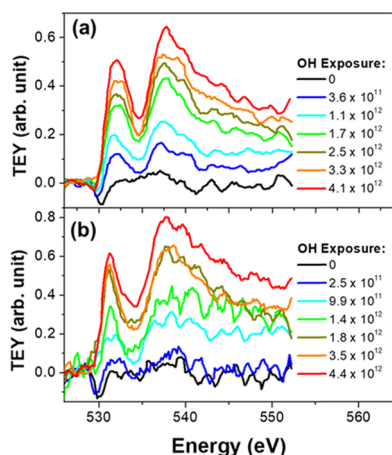


Figure 6. Oxygen K edge XAS spectra of squalane (a) and octacosane (b) particles at different OH exposures. Spectra were normalized to the pre-edge intensity (526–528 eV).

normalized to the intensity between 526 and 528 eV, which arises from the tailing edge of the carbon K edge absorption. Because of the short EAL of low KE photoelectrons, the pre-edge intensity has previously been reported to be proportional to the particle surface area (as measured by the SMPS).⁵¹ Similar to the oxygen K edge XAS spectra observed during squalene ozonolysis, two peaks are observed to grow in with increasing OH exposure.⁵¹ The peak at $\sim 532 \text{ eV}$ is slightly red-shifted in octacosane compared to squalane. The reason for this shift is unclear. It could arise from different molecular species (which are predicted to arise from differences in particle diffusion rates)²⁵ or from differences in intermolecular

bonding, since XAS probes unoccupied molecular orbitals and Rydberg states that are very diffuse and sensitive to the bonding environment.

Because the oxygen K edge XAS spectra were normalized by scaling each spectrum by the pre-edge intensity (526–528 eV), which arises from extended carbon K edge absorption, the intensities in the spectra are directly proportional to the O/C ratios at the surface. The calibration factor to relate XAS intensity to O/C ratio was determined using data from both squalene ozonolysis and squalane oxidation. The change in the O/C ratio with increasing squalene ozonolysis was directly measured using XPS. The measured O/C ratio was related to the peak intensities in the oxygen K edge XAS spectra.⁵¹ In this work, XPS was used to directly measure the O/C ratio of squalane particles as they were oxidized. Using this XPS data, the O/C ratio at each OH exposure shown in Figure 6a was determined. Plotting the O/C ratio as a function of oxygen K edge XAS peak intensity for both squalene ozonolysis and squalane oxidation yields a linear relationship (Supporting Information, Figure S3). Thus, using this linear relationship between oxygen XAS intensity and O/C ratio, we can obtain the chemical composition of the surface of squalane and octacosane particles with increasing heterogeneous oxidation.

The change in the O/C ratio for squalane and octacosane is shown in Figure 7a. Using eq 2, the rate constants for the change in O/C ratio at the surfaces of squalane and octacosane are $(3.0 \pm 0.9) \times 10^{-13}$ and $(8.6 \pm 1.2) \times 10^{-13} \text{ cm}^3 \text{ molecule}^{-1} \text{ s}^{-1}$, respectively. As with the carbon K edge XAS spectra, even though the bulk composition of octacosane changes $\sim 10\times$ more slowly than that of squalane, the surface O/C ratio increases $\sim 3\times$ faster. These rate constants are in

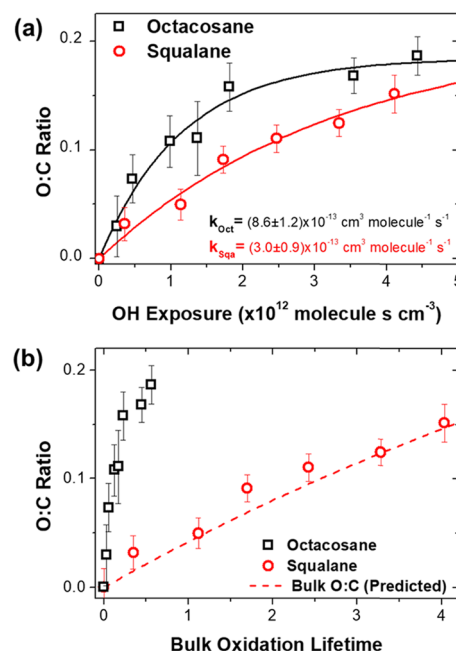


Figure 7. (a) Measured surface O/C ratio for squalane particles (red circles) and octacosane particles (black squares) at different OH exposures. The data were fit to eq 2 to determine the rate of change and the maximum O/C ratio. (b) Measured surface O/C ratio for squalane and octacosane particles at different bulk oxidation lifetimes. Bulk oxidation lifetime was calculated using the bulk AMS measurements and eq 3. The dashed red line shows the bulk O/C ratio predicted for squalane from previous AMS measurements.⁷⁰

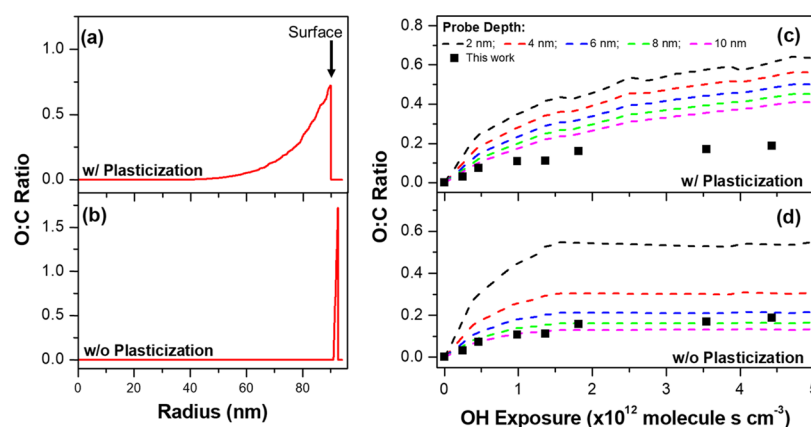


Figure 8. (a, b) Internal distribution of the O/C ratio for triacontane particle with an initial radius of 190 nm after it has been heterogeneously oxidized at an OH exposure of 5.0×10^{12} molecule $s^{-1} cm^{-3}$. The distribution from the model that includes plasticization is shown in (a). The distribution from the model that keeps diffusion constant is shown in (b). (c, d) Estimates of the O/C ratio that would be measured with different probe depths (as determined by electron attenuation lengths). The experimental surface O/C ratios are overlaid (black squares). The changing surface composition with the plasticization model is shown in (c), and the changing surface composition with the constant diffusion model is shown in (d).

good agreement with those describing the spectral changes in the carbon K edge XAS spectra shown in Figure 5, which is a good internal check of our spectra analysis approach.

To directly compare the growth of the surface O/C ratio in the two particles, OH exposure was converted to bulk oxidation lifetimes using the effective uptake coefficient of squalane and octacosane from the AMS measurements. A bulk oxidation lifetime is the number of reactive OH collisions divided by the total number of molecules in the particle. From the second-order reaction rate constant (k_1) describing the decay of the molecular ion, the number of lifetimes is

$$\text{lifetimes} = k_1 \langle \text{OH} \rangle_t \cdot t \quad (3)$$

Figure 7b shows that over the range of OH exposures measured here, the squalane reacts up to ~ 4 lifetimes, whereas octacosane only up to ~ 0.5 lifetime. By plotting the O/C ratio measured with photoemission as a function of bulk oxidation lifetime, the change in the surface composition is related to the change in the bulk composition. The dashed red line in Figure 7b shows the predicted bulk O/C ratio as a function of OH exposure for squalane based on previous results.⁷⁰ For squalane, the bulk values and the surface O/C values are in good agreement, providing strong evidence that the particle is well-mixed. However, the surface O/C ratio for octacosane increases much more rapidly than that of squalane for similar changes in bulk composition. The surface of octacosane reaches its maximum O/C ratio after ~ 0.4 bulk oxidation lifetime (i.e., 35% of octacosane in the particle reacts). Assuming that only octacosane at the surface reacts and there is no internal diffusion, this leads to a ca. 12 nm oxidative crust on the particle (based on estimates of oxidized organic carbon density).⁷⁹

The maximum possible O/C ratios at the particle surfaces were calculated from eq 2 to be 0.21 ± 0.04 and 0.19 ± 0.01 for squalane and octacosane, respectively. The bulk O/C ratios for squalane and triacontane ($C_{30}H_{62}$, a linear hydrocarbon that is assumed to behave identically to octacosane) have been measured previously at very high OH exposures. In this previous measurement, the bulk O/C ratio for squalane was measured to increase to ~ 0.3 after 16 bulk oxidation lifetimes.⁷⁰ This is significantly larger than the maximum O/

C ratio predicted here, presumably due to the limited number of bulk oxidation lifetimes (i.e., a plateau O/C ratio was not achieved for squalane).

In contrast with squalane, the surface composition of octacosane reached a steady value with the OH exposures used here. Previous modeling results have predicted that as I_{RD} increases, the particle starts eroding as fragmentation dominates the overall chemistry, and ketones and carboxylic acids accumulate at the surface.²⁶ In addition, previous measurements have found the bulk O/C ratio for triacontane to increase to >0.9 with an OH exposure of 1×10^{13} molecule $s^{-1} cm^{-3}$.⁶⁴ This is significantly different than what is observed here (maximum surface O/C ratio of 0.19 ± 0.01). Additionally, no products were observed in the bulk AMS measurements reported here that would be consistent with such a large bulk O/C ratio (Figure 2d). The bulk elemental composition in previous studies was determined indirectly using a high-resolution AMS with an electron impact ionization source.⁸² A recent report has summarized the change in average carbon oxidation state with increasing OH exposure for many different particles (from solid to liquid, saturated to unsaturated, etc.).⁶³ Despite its small effective uptake coefficient and low bulk reactivity, triacontane particles were reported to have the largest and fastest change in bulk chemical composition when compared to any other type of particle measured. It is possible that particle morphology, environmental conditions (such as RH), size and plasticization (discussed below) could all impact how particle composition evolves with increased heterogeneous oxidation. However, it is unclear how to understand the differences between the particle compositions measured here and in previous results.

A reaction-diffusion model for the heterogeneous oxidation of triacontane by OH was created to try to understand the previous bulk measurements.⁶⁴ The only way to obtain the large bulk O/C ratios was to assume that the particles plasticized and diffusion time scales in the particle decreased with increasing oxidation (i.e., I_{RD} decreased). Plasticization was built into the model by assuming that reaction products had a larger diffusion coefficient than that of triacontane. With plasticization of the particle, the internal mixing time scales were faster than would be expected from the self-diffusion

coefficient of pure triacontane. As a result, reaction products diffused faster, and the particle was more homogeneously oxidized. When diffusion in the particle was kept constant at the self-diffusion coefficient of triacontane, only the top ~ 1 nm at the surface was oxidized, and a highly oxidized crust was formed. Because products from oxidation were confined to the surface, the maximum bulk O/C ratio under these conditions was ~ 0.1 (which did not support the previous bulk measurements).⁶⁴

To understand the results presented here, two additional triacontane simulations were run using the particle diameter and at the OH exposures measured here. As previously described, heterogeneous oxidation is simulated using a multicompartment model with built-in diffusion pathways. Heterogeneous chemistry, bulk chemistry, diffusion, and evaporation rates are all explicitly stated using literature values when possible.⁶⁴ The model was run using Kinetoscope, which is a stochastic kinetics simulator.⁸³ At each OH exposure, the spatially resolved distribution of the O/C ratios was recorded. The internal distributions of the O/C ratio at an OH exposure of 5.0×10^{12} molecule s cm^{-3} using the plasticization model and the constant diffusion model are shown in Figure 8a,b, respectively. As discussed, oxygenated molecules are allowed to diffuse faster in the plasticization model. As a result, the contrast between the surface and bulk composition is not as extreme as it is in the constant diffusion model.

The EALs in organic nanoparticles for electrons with >2 eV KE were previously measured to be ~ 3 – 4 nm.⁵² Thus, a depth-averaged O/C ratio can be calculated from each of the simulations using estimates of the EAL (i.e., the experimental probing depth). From the simulated distribution of O/C ratios [OC(r)], the depth-averaged O/C ratio (OC_{*m*}) obtained by XAS is predicted to be

$$\text{OC}_m = \int_0^R \text{OC}(r) e^{-r/\text{EAL}} dr / \int_0^R e^{-r/\text{EAL}} dr \quad (4)$$

where R is the radius of the particle and r is the distance from the surface of the particle. At longer EALs, the XAS probe is less surface sensitive, and more material from the core of the particle is probed. The depth-averaged O/C ratios calculated using different estimated EALs (2, 4, 6, 8, and 10 nm) are shown in Figure 8c,d for the plasticization and constant diffusion models, respectively.

With plasticization, oxidized reaction products can diffuse faster, which results in a less steep chemical gradient within the particle (as shown in Figure 8a). Because new reaction products are still probed at longer EALs, changing the EAL has less of an effect on changing the depth-averaged O/C ratio. For example, at an OH exposure of 5×10^{12} molecule s cm^{-3} , the depth-averaged O/C ratio only decreases from 0.65 to 0.40 when the EAL increases from 2 to 10 nm. The experimental O/C ratios measured with the XAS probe are overlaid on the depth-averaged O/C ratios from the plasticization model in Figure 8c. As expected, the plasticization model (which more closely fits the previous bulk measurements) over-predicts O/C ratio at all estimated EALs. Additionally, the depth-averaged O/C ratios continuously increase over the range of OH exposures simulated. This does not match the functional form of the experimental data observed here, which reaches a plateau at OH exposures larger than 1×10^{12} molecule s cm^{-3} .

Without plasticization, diffusion is uniformly slow, and reaction products are confined to the interface (as shown in Figure 8b). Even though the model predicts O/C ratios that

are >1 at the surface of the particle, the measured O/C ratio decreases significantly when contributions from the subsurface of the particle are included. Because the oxidized layer is only ~ 1 nm thick. For example, at an OH exposure of 5×10^{12} molecule s cm^{-3} , the depth-averaged O/C ratio decreases from 0.56 to 0.12 when the EAL increases from 2 to 10 nm. The experimental O/C ratios are overlaid on the depth-averaged O/C ratios from the constant diffusion model in Figure 8d. This model accurately predicts the measured O/C ratio assuming an EAL of ~ 8 nm, which is reasonable given the strong material dependence on electron scattering at low KEs.⁵² In addition, the depth-averaged O/C ratios plateau over the range of OH exposures simulated, because all of the oxygenated species in the particle are probed at each EAL. This matches the functional form of the experimental data. Thus, the experimental results measured here suggest that aerosol particles composed of long linear hydrocarbons form a highly oxidized crust when they are heterogeneously oxidized, suggesting that an extremely steep chemical gradient is formed within the particle.

IV. CONCLUSIONS

Photoemission spectroscopy was used to study the changing surface composition and the formation of chemical gradients during a heterogeneous reaction. The heterogeneous oxidations of both highly viscous octacosane and liquid squalane particles were compared using both bulk and surface measurements. In bulk measurements, pure octacosane particles were found to react much more slowly than pure squalane particles. In mixtures of octacosane and squalane, the reaction kinetics was dependent on the initial particle composition. When the composition of squalane was high ($x_{\text{sqa}} > 0.8$), diffusion was fast relative to the reaction frequency, and octacosane and squalane reacted with the same fast rates (i.e., $I_{\text{RD}} \ll 1$). As the squalane composition decreased ($0.6 < x_{\text{sqa}} < 0.8$), diffusion started to slow relative to reaction frequency, and octacosane and squalane reacted with the same slower rates (i.e., $I_{\text{RD}} \sim 1$). At low squalane composition ($x_{\text{sqa}} < 0.6$), squalane and octacosane reaction rates diverged and approached the values measured for their pure states, due to phase separation.

The formation of chemical gradients in the particles was measured using XAS at the carbon and oxygen K edges. In these surface sensitive probes, octacosane appeared to heterogeneously react significantly faster than squalane particles, demonstrating that even though the bulk composition of octacosane changed slowly, the surface composition changed much more rapidly. Using the oxygen K edge XAS spectra, the change in the O/C ratio of the surface region could be probed directly. From the kinetics of the O/C ratio, the data reported here suggest that diffusion in the octacosane particle remains very slow and only the molecules at the surface of the particle react, creating a highly oxidized crust around an unoxidized core. This conclusion is supported by the bulk AMS measurements reported here, wherein products of heterogeneous oxidation were below the detection limit. The conclusion is also supported by previous work looking at the products of heterogeneous oxidation of octacosane. This work found that only the ends of the octacosane molecule reacted, suggesting that the molecules were frozen at the particle's surface.¹⁹ The measurements reported here suggest that the bulk O/C ratio of octacosane particles does not increase as rapidly as that of liquid squalane particles.

Previous work looking at heterogeneous oxidation has observed much larger changes in the bulk composition of particles composed of linear alkanes.^{63,64} The kinetic model created in this previous work could explain the data measured here by assuming that particles do not plasticize with increased oxidation.⁶⁴ The differences between the previous measurements and those reported here cannot be readily rationalized, but particle morphology or some other environmental factor (such as relative humidity) could play a role in either promoting or inhibiting plasticization.

Ultimately, this work demonstrates that diffusion limitations can create particles with highly oxidized surfaces at relatively low oxidant exposures. By changing the chemical nature of the interface, it is expected that the atmospheric fate of these diffusion-limited particles will change.

■ ASSOCIATED CONTENT

📄 Supporting Information

The Supporting Information is available free of charge on the ACS Publications website at DOI: [10.1021/acs.jpca.9b04507](https://doi.org/10.1021/acs.jpca.9b04507).

Measuring effective uptake coefficients in mixtures; OH radical reaction mechanism; reference carbon K edge XAS spectra; O/C ratio calibration curve from oxygen K edge XAS spectra (PDF)

■ AUTHOR INFORMATION

Corresponding Author

*E-mail: krwilson@lbl.gov. Phone: (510) 495-2474.

ORCID

Michael I. Jacobs: [0000-0003-3682-0409](https://orcid.org/0000-0003-3682-0409)

Bo Xu: [0000-0002-1120-3423](https://orcid.org/0000-0002-1120-3423)

Oleg Kostko: [0000-0003-2068-4991](https://orcid.org/0000-0003-2068-4991)

Frances A. Houle: [0000-0001-5571-2548](https://orcid.org/0000-0001-5571-2548)

Musahid Ahmed: [0000-0003-1216-673X](https://orcid.org/0000-0003-1216-673X)

Kevin R. Wilson: [0000-0003-0264-0872](https://orcid.org/0000-0003-0264-0872)

Notes

The authors declare no competing financial interest.

■ ACKNOWLEDGMENTS

This work is supported by the Chemical Sciences Geosciences and Biosciences Division of the Office of Basic Energy Sciences of the U.S. Department of Energy under Contract No. DE-AC02-05CH11231. M.I.J. was supported by a NSF Graduate Research Fellowship under DGE-1106400. F.A.H. and A.A.W. were supported by the Laboratory Directed Research and Development program at Lawrence Berkeley National Laboratory under U.S. Department of Energy Office of Science, Office of Basic Energy Sciences under Contract No. DE-AC02-05CH11231. This research used resources of the Advanced Light Source, which is a DOE Office of Science User Facility under contract no. DE-AC02-05CH11231.

■ REFERENCES

- (1) Virtanen, A.; Joutsensaari, J.; Koop, T.; Kannosto, J.; Yli-Pirilä, P.; Leskinen, J.; Mäkelä, J. M.; Holopainen, J. K.; Pöschl, U.; Kulmala, M.; et al. An Amorphous Solid State of Biogenic Secondary Organic Aerosol Particles. *Nature* **2010**, *467*, 824–827.
- (2) Roth, C. M.; Goss, K. U.; Schwarzenbach, R. P. Sorption of a Diverse Set of Organic Vapors to Diesel Soot and Road Tunnel Aerosols. *Environ. Sci. Technol.* **2005**, *39*, 6632–6637.
- (3) Koop, T.; Bookhold, J.; Shiraiwa, M.; Pöschl, U. Glass Transition and Phase State of Organic Compounds: Dependency on Molecular

Properties and Implications for Secondary Organic Aerosols in the Atmosphere. *Phys. Chem. Chem. Phys.* **2011**, *13*, 19238–19255.

- (4) Reid, J. P.; Bertram, A. K.; Topping, D. O.; Laskin, A.; Martin, S. T.; Petters, M. D.; Pope, F. D.; Rovelli, G. The Viscosity of Atmospherically Relevant Organic Particles. *Nat. Commun.* **2018**, *9*, No. 956.

- (5) Jimenez, J. L.; Canagaratna, M. R.; Donahue, N. M.; Prevot, A. S. H.; Zhang, Q.; Kroll, J. H.; DeCarlo, P. F.; Allan, J. D.; Coe, H.; Ng, N. L.; et al. Evolution of Organic Aerosols in the Atmosphere. *Science* **2009**, *326*, 1525–1529.

- (6) Farmer, D. K.; Cappa, C. D.; Kreidenweis, S. M. Atmospheric Processes and Their Controlling Influence on Cloud Condensation Nuclei Activity. *Chem. Rev.* **2015**, *115*, 4199–4217.

- (7) Ruehl, C. R.; Davies, J. F.; Wilson, K. R. An Interfacial Mechanism for Cloud Droplet Formation on Organic Aerosols. *Science* **2016**, *351*, 1447.

- (8) Pajunoja, A.; Lambe, A. T.; Hakala, J.; Rastak, N.; Cummings, M. J.; Brogan, J. F.; Hao, L.; Paramonov, M.; Hong, J.; Prisle, N. L.; et al. Adsorptive Uptake of Water by Semisolid Secondary Organic Aerosols in the atmosphere. *Nat. Geosci.* **2014**, *42*, 1–6.

- (9) Gray Bé, A.; Upshur, M. A.; Liu, P.; Martin, S. T.; Geiger, F. M.; Thomson, R. J. Cloud Activation Potentials for Atmospheric α -Pinene and β -Caryophyllene Ozonolysis Products. *ACS Cent. Sci.* **2017**, *3*, 715–725.

- (10) Chan, M. N.; Zhang, H.; Goldstein, A. H.; Wilson, K. R. Role of Water and Phase in the Heterogeneous Oxidation of Solid and Aqueous Succinic Acid Aerosol by Hydroxyl Radicals. *J. Phys. Chem. C* **2014**, *118*, 28978–28992.

- (11) Slade, J. H.; Knopf, D. A. Multiphase OH Oxidation Kinetics of Organic Aerosol: The Role of Particle Phase State and Relative Humidity. *Geophys. Res. Lett.* **2014**, *41*, 5297–5306.

- (12) Arangio, A. M.; Slade, J. H.; Berkemeier, T.; Pöschl, U.; Knopf, D. A.; Shiraiwa, M. Multiphase Chemical Kinetics of OH Radical Uptake by Molecular Organic Markers of Biomass Burning Aerosols: Humidity and Temperature Dependence, Surface Reaction, and Bulk Diffusion. *J. Phys. Chem. A* **2015**, *119*, 4533–4544.

- (13) Moise, T.; Rudich, Y. Reactive Uptake of Ozone by Aerosol-associated Unsaturated Fatty Acids: Kinetics, Mechanism, and Products. *J. Phys. Chem. A* **2002**, *106*, 6469–6476.

- (14) Davies, J. F.; Wilson, K. R. Nanoscale Interfacial Gradients Formed by the Reactive Uptake of OH Radicals onto Viscous Aerosol Surfaces. *Chem. Sci.* **2015**, *6*, 7020–7027.

- (15) Shiraiwa, M.; Ammann, M.; Koop, T.; Pöschl, U. Gas Uptake and Chemical Aging of Semisolid Organic Aerosol Particles. *Proc. Natl. Acad. Sci. U.S.A.* **2011**, *108*, 11003–11008.

- (16) Berkemeier, T.; Steimer, S. S.; Krieger, U. K.; Peter, T.; Pöschl, U.; Ammann, M.; Shiraiwa, M. Ozone Uptake on Glassy, Semi-Solid and Liquid Organic Matter and the Role of Reactive Oxygen Intermediates in Atmospheric Aerosol Chemistry. *Phys. Chem. Chem. Phys.* **2016**, *18*, 12662–12674.

- (17) Steimer, S. S.; Berkemeier, T.; Gilgen, A.; Krieger, U. K.; Peter, T.; Shiraiwa, M.; Ammann, M. Shikimic Acid Ozonolysis Kinetics of the Transition from Liquid Aqueous Solution to Highly Viscous Glass. *Phys. Chem. Chem. Phys.* **2015**, *17*, 31101–31109.

- (18) Marshall, F. H.; Berkemeier, T.; Shiraiwa, M.; Nandy, L.; Ohm, P. B.; Dutcher, C. S.; Reid, J. P. Influence of Particle Viscosity on Mass Transfer and Heterogeneous Ozonolysis Kinetics in Aqueous-Sucrose-Maleic Acid Aerosol. *Phys. Chem. Chem. Phys.* **2018**, *20*, 15560–15573.

- (19) Ruehl, C.; Nah, T.; Isaacman, G.; Worton, D.; Chan, A. W. H.; Kolesar, K. R.; Cappa, C. D.; Goldstein, A. H.; Wilson, K. R. The Influence of Molecular Structure and Aerosol Phase on the Heterogeneous Oxidation of Normal and Branched Alkanes by OH. *J. Phys. Chem. A* **2013**, *117*, 3990–4000.

- (20) Kuwata, M.; Martin, S. T. Phase of Atmospheric Secondary Organic Material Affects its Reactivity. *Proc. Natl. Acad. Sci. U.S.A.* **2012**, *109*, 17354–17359.

- (21) Zhou, S.; Shiraiwa, M.; McWhinney, R. D.; Pöschl, U.; Abbatt, J. P. D. Kinetic Limitations in Gas-Particle Reactions Arising from

Slow Diffusion in Secondary Organic Aerosol. *Faraday Discuss.* **2013**, *165*, 391–406.

(22) Allan, M.; Bagot, P. A. J.; Westacott, R. E.; Costen, M. L.; Mckendrick, K. G. Influence of Molecular and Supramolecular Structure on the Gas-Liquid Interfacial Reactivity of Hydrocarbon Liquids with O (3P) Atoms. *J. Phys. Chem. C* **2008**, *112*, 1524–1532.

(23) Lee, L.; Wilson, K. The Reactive–Diffusive Length of OH and Ozone in Model Organic Aerosols. *J. Phys. Chem. A* **2016**, *120*, 6800–6812.

(24) Houle, F. A.; Hinsberg, W. D.; Wilson, K. R. Oxidation of a Model Alkane Aerosol by OH Radical: The Emergent Nature of Reactive Uptake. *Phys. Chem. Chem. Phys.* **2015**, *17*, 4412–4423.

(25) Houle, F. A.; Wiegel, A. A.; Wilson, K. R. Changes in Reactivity as Chemistry Becomes Confined to an Interface. The Case of Free Radical Oxidation of C₃₀H₆₂ Alkane by OH. *J. Phys. Chem. Lett.* **2018**, *9*, 1053–1057.

(26) Houle, F. A.; Wiegel, A. A.; Wilson, K. R. Predicting Aerosol Reactivity Across Scales: from the Laboratory to the Atmosphere. *Environ. Sci. Technol.* **2018**, *52*, 13774–13781.

(27) Pfrang, C.; Shiraiwa, M.; Pöschl, U. Chemical Ageing and Transformation of Diffusivity in Semi-Solid Multi-Component Organic Aerosol Particles. *Atmos. Chem. Phys.* **2011**, *11*, 7343–7354.

(28) Jayne, J. T.; Leard, D. C.; Zhang, X.; Davidovits, P.; Smith, K.; Kolb, C. E.; Worsnop, D. R. Development of an Aerosol Mass Spectrometer for Size and Composition Analysis of Submicron Particles. *Aerosol Sci. Technol.* **2000**, *33*, 49–70.

(29) Maria, S. F.; Russell, L. M.; Gilles, M. K.; Myneni, S. C. B. Organic Aerosol Growth Mechanisms and Their Climate-Forcing Implications. *Science* **2004**, *306*, 1921–1924.

(30) Laskin, A.; Iedema, M. J.; Cowin, J. P. Time-Resolved Aerosol Collector for CCSEM/EDX Single-Particle Analysis. *Aerosol Sci. Technol.* **2003**, *37*, 246–260.

(31) Pratt, K. A.; Prather, K. A. Mass Spectrometry of Atmospheric Aerosols—Recent Developments and Applications. Part I: Off-line Mass Spectrometry Techniques. *Mass Spectrom. Rev.* **2012**, *31*, 1–16.

(32) Lim, C. Y.; Browne, E. C.; Sugrue, R. A.; Kroll, J. H. Rapid Heterogeneous Oxidation of Organic Coatings on Submicron Aerosols. *Geophys. Res. Lett.* **2017**, *44*, 2949–2957.

(33) Chan, M. N.; Nah, T.; Wilson, K. R. Real Time in Situ Chemical Characterization of Sub-Micron Organic Aerosols Using Direct Analysis in Real Time Mass Spectrometry (DART-MS): The Effect of Aerosol Size and Volatility. *Analyst* **2013**, *138*, 3749.

(34) Nah, T.; Chan, M.; Leone, S. R.; Wilson, K. R. Real Time in Situ Chemical Characterization of Submicrometer Organic Particles using Direct Analysis in Real Time-Mass Spectrometry. *Anal. Chem.* **2013**, *85*, 2087–2095.

(35) Zhao, Y.; Fairhurst, M. C.; Wingen, L. M.; Perraud, V.; Ezell, M. J.; Finlayson-Pitts, B. J. New Insights Into Atmospherically Relevant Reaction Systems Using Direct Analysis in Real-Time Mass Spectrometry (DART-MS). *Atmos. Meas. Tech.* **2017**, *10*, 1373–1386.

(36) Kumbhani, S.; Longin, T.; Wingen, L. M.; Kidd, C.; Perraud, V.; Finlayson-Pitts, B. J. New Mechanism of Extractive Electrospray Ionization Mass Spectrometry for Heterogeneous Solid Particles. *Anal. Chem.* **2018**, *90*, 2055–2062.

(37) Wingen, L. M.; Finlayson-Pitts, B. J. Probing Surfaces of Atmospherically Relevant Organic Particles by Easy Ambient Sonic-Spray Ionization Mass Spectrometry (EASI-MS). *Chem. Sci.* **2019**, *10*, 884–897.

(38) Wu, Y.; Li, W.; Xu, B.; Li, X.; Wang, H.; McNeill, V. F.; Rao, Y.; Dai, H. L. Observation of Organic Molecules at the Aerosol Surface. *J. Phys. Chem. Lett.* **2016**, *7*, 2294–2297.

(39) Ebben, C. J.; Ault, A. P.; Ruppel, M. J.; Ryder, O. S.; Bertram, T. H.; Grassian, V. H.; Prather, K. A.; Geiger, F. M. Size-Resolved Sea Spray Aerosol Particles Studied by Vibrational Sum Frequency Generation. *J. Phys. Chem. A* **2013**, *117*, 6589–6601.

(40) Martinez, I. S.; Peterson, M. D.; Ebben, C. J.; Hayes, P. L.; Artaxo, P.; Martin, S. T.; Geiger, F. M. On Molecular Chirality Within Naturally Occurring Secondary Organic Aerosol Particles from the

Central Amazon Basin. *Phys. Chem. Chem. Phys.* **2011**, *13*, 12114–12122.

(41) Wilson, K. R.; Bluhm, H.; Ahmed, M. Aerosol Photoemission. In *Fundamentals and Applications in Aerosol Spectroscopy*; Signorell, R., Reid, J. P., Eds.; CRC Press: Boca Raton, FL, 2011; pp 367–400.

(42) Wilson, K. R.; Peterka, D. S.; Jimenez-Cruz, M.; Leone, S. R.; Ahmed, M. VUV Photoelectron Imaging of Biological Nanoparticles: Ionization Energy Determination of Nanophase Glycine and Phenylalanine-Glycine-Glycine. *Phys. Chem. Chem. Phys.* **2006**, *8*, 1884–1890.

(43) Wilson, K. R.; Zou, S.; Shu, J.; Rühl, E.; Leone, S. R.; Schatz, G. C.; Ahmed, M. Size-Dependent Angular Distributions of Low-Energy Photoelectrons Emitted from NaCl Nanoparticles. *Nano Lett.* **2007**, *7*, 2014–2019.

(44) Lin, P.-C.; Wu, Z.-H.; Chen, M.-S.; Li, Y.-L.; Chen, W.-R.; Huang, T.-P.; Lee, Y.; Wang, C. C. Interfacial Solvation and Surface pH of Phenol and Dihydroxybenzene Aqueous Nanoaerosols Unveiled by Aerosol VUV Photoelectron Spectroscopy. *J. Phys. Chem. B* **2017**, *121*, 1054–1067.

(45) Woods, E.; Konys, C. A.; Rossi, S. R. Photoemission of Iodide from Aqueous Aerosol Particle Surfaces. *J. Phys. Chem. A* **2019**, *123*, 2901–2907.

(46) Berg, M. J.; Wilson, K. R.; Sorensen, C. M.; Chakrabarti, A.; Ahmed, M. Discrete Dipole Approximation for Low-Energy Photoelectron Emission from NaCl Nanoparticles. *J. Quant. Spectrosc. Radiat. Transfer* **2012**, *113*, 259–265.

(47) Goldmann, M.; Miguel-Sánchez, J.; West, A. H. C.; Yoder, B. L.; Signorell, R. Electron Mean Free Path from Angle-Dependent Photoelectron Spectroscopy of Aerosol Particles. *J. Chem. Phys.* **2015**, *142*, No. 224304.

(48) West, A. H. C.; Yoder, B. L.; Signorell, R. Size-Dependent Velocity Map Photoelectron Imaging of Nanosized Ammonia Aerosol Particles. *J. Phys. Chem. A* **2013**, *117*, 13326–13335.

(49) Shu, J.; Wilson, K. R.; Ahmed, M.; Leone, S. R. Coupling a Versatile Aerosol Apparatus to a Synchrotron: Vacuum Ultraviolet Light Scattering, Photoelectron Imaging, and Fragment Free Mass Spectrometry. *Rev. Sci. Instrum.* **2006**, *77*, No. 043106.

(50) Signorell, R.; Goldmann, M.; Yoder, B. L.; Bodi, A.; Chasovskikh, E.; Lang, L.; Luckhaus, D. Nanofocusing, Shadowing, and Electron Mean Free Path in the Photoemission from Aerosol Droplets. *Chem. Phys. Lett.* **2016**, *658*, 1–6.

(51) Jacobs, M. I.; Xu, B.; Kostko, O.; Heine, N.; Ahmed, M.; Wilson, K. R. Probing the Heterogeneous Ozonolysis of Squalene Nanoparticles by Photoemission. *J. Phys. Chem. A* **2016**, *120*, 8645–8656.

(52) Jacobs, M. I.; Kostko, O.; Ahmed, M.; Wilson, K. R. Low Energy Electron Attenuation Lengths in Core-Shell Nanoparticles. *Phys. Chem. Chem. Phys.* **2017**, *19*, 13372–13378.

(53) Xiong, W.; Hickstein, D. D.; Schnitzenbaumer, K. J.; Ellis, J. L.; Palm, B. B.; Keister, K. E.; Ding, C.; Miaja-Avila, L.; Dukovic, G.; Jimenez, J. L.; et al. Photoelectron Spectroscopy of CdSe Nanocrystals in the Gas Phase: A Direct Measure of the Evanescent Electron Wave Function of Quantum Dots. *Nano Lett.* **2013**, *13*, 2924–2930.

(54) Mysak, E. R.; Starr, D. E.; Wilson, K. R.; Bluhm, H. Note: A Combined Aerodynamic Lens/Ambient Pressure X-ray Photoelectron Spectroscopy Experiment for the On-Stream Investigation of Aerosol Surfaces. *Rev. Sci. Instrum.* **2010**, *81*, No. 016106.

(55) Antonsson, E.; Patanen, M.; Nicolas, C.; Neville, J. J.; Benkoula, S.; Goel, A.; Miron, C. Complete Bromide Surface Segregation in Mixed NaCl/NaBr Aerosols Grown from Droplets. *Phys. Rev. X* **2015**, *5*, No. 011025.

(56) Benkoula, S.; Sublemontier, O.; Patanen, M.; Nicolas, C.; Sirotti, F.; Naitabdi, A.; Gaie-Levrel, F.; Antonsson, E.; Aureau, D.; Ouf, F.-X.; et al. Water Adsorption on TiO₂ Surfaces Probed by Soft X-ray Spectroscopies: Bulk materials vs. Isolated Nanoparticles. *Sci. Rep.* **2015**, *5*, No. 15088.

(57) Antonsson, E.; Langer, B.; Halfpap, I.; Gottwald, J.; Rühl, E. Photoelectron Angular Distribution from Free SiO₂ Nanoparticles as

a Probe of Elastic Electron Scattering. *J. Chem. Phys.* **2017**, *146*, No. 244301.

(58) Meinen, J.; Khasminskaya, S.; Erritt, M.; Leisner, T.; Antonsson, E.; Langer, B.; Rühl, E. Core Level Photoionization on Free Sub-10-nm Nanoparticles Using Synchrotron Radiation. *Rev. Sci. Instrum.* **2010**, *81*, No. 085107.

(59) Sublemontier, O.; Nicolas, C.; Aureau, D.; Patanen, M.; Kintz, H.; Liu, X.; Gaveau, M.; Garrec, J. L.; Robert, E.; Barreda, F.; et al. X-ray Photoelectron Spectroscopy of Isolated Nanoparticles. *J. Phys. Chem. Lett.* **2014**, *5*, 3399–3403.

(60) Kostko, O.; Xu, B.; Jacobs, M. I.; Ahmed, M. Soft X-ray Spectroscopy of Nanoparticles by Velocity Map Imaging. *J. Chem. Phys.* **2017**, *147*, No. 013931.

(61) Xu, B.; Jacobs, M. I.; Kostko, O.; Ahmed, M. Guanidinium Group is Protonated in a Strongly Basic Arginine Solution. *ChemPhysChem* **2017**, *18*, 1503–1506.

(62) Ouf, F.-X.; Parent, P.; Laffon, C.; Marhaba, I.; Ferry, D.; Marcillaud, B.; Antonsson, E.; Benkoula, S.; Liu, X.-J.; Nicolas, C.; et al. First In-Flight Synchrotron X-ray Absorption and Photoemission Study of Carbon Soot Nanoparticles. *Sci. Rep.* **2016**, *6*, No. 36495.

(63) Kroll, J. H.; Lim, C. Y.; Kessler, S. H.; Wilson, K. R. Heterogeneous Oxidation of Atmospheric Organic Aerosol: Kinetics of Changes to the Amount and Oxidation State of Particle-Phase Organic Carbon. *J. Phys. Chem. A* **2015**, *119*, 10767–10783.

(64) Wiegel, A. A.; Liu, M. J.; Hinsberg, W. D.; Wilson, K. R.; Houle, F. A. Diffusive Confinement of Free Radical Intermediates in the OH Radical Oxidation of Semisolid Aerosols. *Phys. Chem. Chem. Phys.* **2017**, *19*, 6814–6830.

(65) Smith, J. D.; Kroll, J. H.; Cappa, C. D.; Che, D. L.; Liu, C. L.; Ahmed, M.; Leone, S. R.; Worsnop, D. R.; Wilson, K. R. The Heterogeneous Reaction of Hydroxyl Radicals with Sub-Micron Squalane Particles: A Model System for Understanding the Oxidative Aging of Ambient Aerosols. *Atmos. Chem. Phys.* **2009**, *9*, 3209–3222.

(66) Atkinson, R.; Baulch, D. L.; Cox, R.; Crowley, J. N.; Hampson, R. F.; Hynes, R. G.; Jenkin, M. E.; Rossi, M. J.; Troe, J. Evaluated Kinetic and Photochemical Data for Atmospheric Chemistry: Volume III – Gas Phase Reactions of Inorganic Halogens. *Atmos. Chem. Phys.* **2007**, *7*, 981–1191.

(67) Gloaguen, E.; Mysak, E. R.; Leone, S. R.; Ahmed, M.; Wilson, K. R. Investigating the Chemical Composition of Mixed Organic-Inorganic Particles by “Soft” Vacuum Ultraviolet Photoionization: The Reaction of Ozone with Anthracene on Sodium Chloride Particles. *Int. J. Mass Spectrom.* **2006**, *258*, 74–85.

(68) Dribinski, V.; Ossadtchi, A.; Mandelshtam, V.; Reisler, H. Reconstruction of Abel-Transformable Images: The Gaussian Basis-Set Expansion Abel Transform Method. *Rev. Sci. Instrum.* **2002**, *73*, 2634.

(69) Wiegel, A.; Wilson, K. R.; Hinsberg, W. D.; Houle, F. Stochastic Methods for Aerosol Chemistry: A Compact Molecular Description of Functionalization and Fragmentation in the Heterogeneous Oxidation of Squalane Aerosol by OH Radicals. *Phys. Chem. Chem. Phys.* **2015**, *17*, 4398–4411.

(70) Kroll, J. H.; Smith, J. D.; Che, D. L.; Kessler, S. H.; Worsnop, D. R.; Wilson, K. R. Measurement of Fragmentation and Functionalization Pathways in the Heterogeneous Oxidation of Oxidized Organic Aerosol. *Phys. Chem. Chem. Phys.* **2009**, *11*, 8005.

(71) Che, D. L.; Smith, J. D.; Leone, S. R.; Ahmed, M.; Wilson, K. R. Quantifying the Reactive Uptake of OH by Organic Aerosols in a Continuous Flow Stirred Tank Reactor. *Phys. Chem. Chem. Phys.* **2009**, *11*, 7885–7895.

(72) Richards-Henderson, N. K.; Goldstein, A. H.; Wilson, K. R. Large Enhancement in the Heterogeneous Oxidation Rate of Organic Aerosols by Hydroxyl Radicals in the Presence of Nitric Oxide. *J. Phys. Chem. Lett.* **2015**, *6*, 4451–4455.

(73) Richards-Henderson, N. K.; Goldstein, A. H.; Wilson, K. R. Sulfur Dioxide Accelerates the Heterogeneous Oxidation Rate of Organic Aerosol by Hydroxyl Radicals. *Environ. Sci. Technol.* **2016**, *50*, 3554–3561.

(74) Katrib, Y.; Biskos, G.; Buseck, P. R.; Davidovits, P.; Jayne, J. T.; Mochida, M.; Wise, M. E.; Worsnop, D. R.; Martin, S. T. Ozonolysis of Mixed Oleic-Acid/Stearic-Acid Particles: Reaction Kinetics and Chemical Morphology. *J. Phys. Chem. A* **2005**, *109*, 10910–10919.

(75) Kwok, E. S. C.; Atkinson, R. Estimation of Hydroxyl Radical Reaction Rate Constants for Gas-Phase Organic Compounds Using a Structure-Reactivity Relationship: An Update. *Atmos. Environ.* **1995**, *29*, 1685–1695.

(76) Heslot, F.; Cazabat, A. M.; Levinson, P. Dynamics of Wetting of Tiny Drops: Ellipsometric Study of the Late Stages of Spreading. *Phys. Rev. Lett.* **1989**, *62*, 1286–1289.

(77) Mysak, E. R.; Smith, J. D.; Ashby, P. D.; Newberg, J. T.; Wilson, K. R.; Bluhm, H. Competitive Reaction Pathways for Functionalization and Volatilization in the Heterogeneous Oxidation of Coronene Thin Films by Hydroxyl Radicals and Ozone. *Phys. Chem. Chem. Phys.* **2011**, *13*, 7554–7564.

(78) Beamson, G.; Briggs, D. *High Resolution XPS of Organic Polymers: The Scienta ESCA300 Database*; John Wiley & Sons, Inc.: Chichester, 1992.

(79) Wilson, K. R.; Smith, J. D.; Kessler, S. H.; Kroll, J. H. The Statistical Evolution of Multiple Generations of Oxidation Products in the Photochemical Aging of Chemically Reduced Organic Aerosol. *Phys. Chem. Chem. Phys.* **2012**, *14*, 1468–1479.

(80) Moffet, R. C.; Henn, T.; Laskin, A.; Gilles, M. K. Automated Chemical Analysis of Internally Mixed Aerosol Particles Using X-ray Spectromicroscopy at the Carbon K-edge. *Anal. Chem.* **2010**, *82*, 7906–7914.

(81) Hitchcock, A. P.; Mancini, D. C. Bibliography and Database of Inner Shell Excitation Spectra of Gas Phase Atoms and Molecules. *J. Electron Spectrosc. Relat. Phenom.* **1994**, *67*, 1–132.

(82) Aiken, A. C.; Decarlo, P. F.; Kroll, J. H.; Worsnop, D. R.; Huffman, J. A.; Docherty, K. S.; Ulbrich, I. M.; Mohr, C.; Kimmel, J. R.; Sueper, D.; et al. O/C and OM/OC Ratios of Primary, Secondary, and Ambient Organic Aerosols with High-Resolution Time-of-Flight Aerosol Mass Spectrometry. *Environ. Sci. Technol.* **2008**, *42*, 4478–4485.

(83) Hinsberg, W. D.; Houle, F. A. Kinetiscope <http://www.hinsberg.net/kinetiscope/> (accessed May 1, 2019).